Impulse coupling measurement of metallic and carbon targets during laser ablation through ballistic pendulum experiments and simulations

C. Le Bras,[1,a)] L. Berthe,[2] L. Videau,[3] S. Baton,[4] M. Boustie,[5] S. Boyer,[6] C. Rousseaux,[7] E. Brambrink,[8] J.-M. Chevalier,[1] J. Houy,[4] B. Aubert,[1] B. Jodar,[7] D. Loison,[9] and D. Hébert[1]

AFFILIATIONS

[1]CEA, DAM, CESTA, F-33114 Le Barp, France
[2]CNRS, Laboratoire PIMM, Arts et Métiers ParisTech, 75013 Paris, France
[3]Université Paris-Saclay, CEA, LMCE, F-91680 Bruyère-Le-Châtel, France
[4]LULI, CNRS-Ecole Polytechnique-CEA-Sorbonne Université, Palaiseau, France
[5]CNRS-PPRIME, ISAE ENSMA, Futuroscope, France
[6]CNRS-CEMEF, Mines ParisTech PSL, Sophia Antipolis, France
[7]CEA, DAM, DIF, F-91297 Arpajon, France
[8]European XFEL, Holzkoppel 4, 22869 Hamburg, Germany
[9]Univ. Rennes, CNRS, IPR (Institut de Physique de Rennes)—UMR 6251, F-35000 Rennes, France

[a)]Author to whom correspondence should be addressed: corentin.lebras@hotmail.fr

ABSTRACT

Laser ablation propulsion and orbit cleaning are developing areas of research. The general aim of laser-based techniques applied to this field is to maximize the momentum transfer produced by a laser shot. This work presents results from ballistic pendulum experiments under vacuum on aluminum, copper, tin, gold, and porous graphite targets. The work has focused on the metrology of the laser experiments to ensure good stability over a wide range of laser parameters (laser intensity ranging from 4 GW/cm^2 to 8.7 TW/cm^2, pulse duration from 80 ps to 15 ns, and wavelengths of 528 or 1057 nm). The results presented compile data from three experimental campaigns spanning from 2018 to 2021 on two different laser platforms and using different pulse durations, energies, and wavelengths. The study is complemented by the simulation of the momentum from the mono-dimensional Lagrangian code ESTHER. The first part of this work gives a detailed description of the experimental setup used, the ESTHER code, and the treatment of the simulations. The second part focuses on the experimental results. The third part describes the simulation results and provides a comparison with the experimental data. The last part presents possible improvements for future work on the subject.

I. INTRODUCTION

Since the launch of the first satellites in the 1950s, the number of objects in low Earth orbit (LEO) has continued to grow and now exceeds 100×10^6 for those larger than 1 mm. Of these, about 34 000 are larger than 10 cm and only 20 000 are documented, while only 1500 satellites are maneuverable.[1] This raises the question of collisions between objects, be they satellites or debris. Considering that these objects can travel in space at speeds in the tens of km/s range, even a 1 mm of debris can cause significant damage to a working satellite.[2] One way to protect spacecraft is to install whipple shields to mitigate potential collisions, but this type of solution is only effective for small impactors, while making the global structure heavier and risking the creation of new debris in the event of a collision.[3–6] For this type of application involving hypervelocity impacts (HVIs), studies are realized mainly with gas

guns. However, the maximum projectile velocities achieved are <10 km/s. Laser, on the other hand, offers several advantages over gas guns for this type of study: shots can be made more quickly, allowing more experiments to be performed, and the shocks produced are comparable to hypervelocity impacts with velocities equivalent to those found in space debris collisions.[7–12] Another area of laser shock development in the space domain is Laser Ablation Propulsion (LAP). The idea was first described by Kantrowitz in 1972[13] and is similar to the hypervelocity impact experiments in that the surface of an object is ablated to create a thrust that is used to propel the object.[14,15] A detailed description of the process and its history can be found in Phipps' work.[16]

In both of these applications, the key parameter is the momentum Q (N s), which is imparted to the shocked material by the conservation of momentum. The momentum is calculated with

$$Q = \int T(t)\,\mathrm{dt}, \tag{1}$$

where T is the thrust generated in N on the target material.

The total momentum imparted by a laser pulse applied to a material surface consists of several contributions. In addition to the plasma expansion effects, the resulting shock wave ejects solid or liquid debris.[17] The contribution of these ejecta has not been extensively studied in laser experiments, although it may play an important role in the momentum transfer from hypervelocity impacts. In order to be able to investigate the effect of said ejecta, several materials were selected for this study, with different fragmentation (ductile or brittle) and with different debris ejection processes (in the liquid or solid phase).

By knowing both the momentum Q and E, the laser energy in J, the impulse coupling also called mechanical coupling coefficient C_m (N/MW) can be calculated as

$$C_\mathrm{m} = \frac{Q}{E}\,10^6. \tag{2}$$

In LAP or laser deorbiting,[18] knowledge of the momentum imparted by a laser shock, and hence the momentum coupling, is crucial to correctly predict the result of a laser irradiation.

Multiple complex mechanisms can take place during this laser irradiation. First, part of the electromagnetic wave couples to the free electrons of the conduction band, resulting in energy absorption and a temperature rise in the optical skin depth. It is also important to note that the evolution of the laser–matter interaction is a deeply coupled process involving hydrodynamics, heat transfer, and laser absorption. A variety of regimes (such as vaporization, melting, superheating, and phase explosion) can be observed depending on the laser parameters (e.g., fluence, pulse duration, spot size, and beam homogeneity). Nevertheless, Phipps' model[19,20] correlates the momentum coupling to a parameter "$I\lambda\sqrt{\tau}$" (W/m s$^{1/2}$), where I is the laser intensity in W/m^2, λ is the wavelength of the laser used in m, and τ is its pulse duration in s. The model separates the interaction into two regimes, first the vapor regime where the ablation starts to grow, followed by the plasma regime where the plasma is fully formed. The coupling between the two phases is controlled by a weighting function that depends on the ionization fraction in the ablation plume.

In all but one of the experiments considered in this work, the heating rate is high enough to reach temperatures of tens of thousands K, placing the interaction in the plasma regime. The plasma is created at the surface of the sample and expands into the vacuum. The laser wave then propagates through the low-density plasma up to the critical density where the absorbed laser energy in the plasma is transferred by heat conduction toward deeper and denser parts of the material, thereby ablating the target and feeding the expanding plasma. In response to this material ejection, a pressure wave is generated in the sample which ultimately sets it into motion by momentum transfer.

Data are abundant for aluminum using this model because the material properties are well known, but the experiments performed were extracted from old literature with no access to raw data[21–23] for low $I\lambda\sqrt{\tau}$ values, while the literature for high $I\lambda\sqrt{\tau}$ values presented a complex configuration not often seen in other papers in the results obtained.[24] In addition, the datasets are from different lasers with a wide range of parameters, making a proper comparison somewhat difficult. Thus, data with identical experimental protocol but varying laser parameters are scarce.

This paper aimed at experimentally covering a wide range of $I\lambda\sqrt{\tau}$ values with different laser configurations in vacuum, for applications such as LAP and HVI in order to obtain highly accurate results of momentum and momentum coupling calculations from laser pulses focused on a ballistic pendulum using varying intensities and pulse durations (4 GW/cm^2 to 8.7 TW/cm^2 and 80 ps to 15 ns) while operating well-controlled laser systems. The experiments were carried out on the ELFIE and LULI2000 platforms in three experimental campaigns. Photonic Doppler Velocity (PDV) and maximum deflection angle measurements of the ballistic pendulum were used to deduce the momentum imparted by the shockwaves. The resulting dataset was in good agreement with the existing literature on the low energy shots but differed on the high energy ones. These generated results were the basis of the comparison to Phipps' model and the mono-dimensional Lagrangian hydrodynamic code ESTHER.

II. MATERIALS AND METHODS

A. Laser facilities

The experiments were carried out in three campaigns over four years. Two lasers have been used, both located at LULI (Laboratoire pour l'Utilisation des Lasers Intenses).[11,25] All the experiments were realized under a 10^{-2} to 10^{-3} mbar vacuum to limit the dampening of the pendulum signal as well as not be hindered by breakdown plasmas in air when using high laser intensities.

- The ELFIE laser system was operated with two different pulse durations, both with a Gaussian shape and full width half maximum (FWHM) of 80 and 560 ps, respectively. Two harmonics of laser crystal were also used (1ω: 1057 nm and 2ω: 528 nm). The beams were focused with a 300 mm off axis parabola for the short pulse and a 700 mm lens for the long pulse, giving

a spot size of 4.6 and 5.5 mm, respectively. The resulting laser intensities ranged from 4 to 860 GW/cm^2.

- The LULI2000 laser is a nanosecond laser operating at 1053 nm. The pulses were focused on the target to form a 0.9 mm focal spot with a diffractive optical element (DOE) used to homogenize the energy distribution. 15 ns short-rise time pulses were used during the experiments. The laser is divided into two chains called "North" and "South," each of which was characterized and alternated in order to reduce the delay between shots due to cooldown. The laser intensities used for the experiment ranged from 1.2 to 8.7 TW/cm^2. Two campaigns took place on this platform and will be denoted LULI2020 and LULI2021.

The main difference between the two laser platforms lies in their widely different pulse durations (ps and ns range). An 80 ps pulse from the ELFIE platform was not expected to produce liquid or solid ejecta, whereas the 560 ps pulses might have done so, being close to the ns range. On the contrary, the shots from the LULI2000 platform were expected to induce the formation of both plasma and ejecta. For both laser systems, the laser spot size was measured using CCD cameras. The pulse durations for the LULI2020 and LULI2021 campaigns and the 560 ps shots from the ELFIE2018 campaign were characterized by recording a temporal pulse profile with a photodiode placed in an optical leak, while the 80 ps shots from the ELFIE2018 campaign were recorded with a streak camera.

Figure 1 shows an example of the pulse profiles obtained for the two laser systems, the first being from the LULI2000 laser with a pulse duration of 15 ns. The profile used for the simulations was a smoothed one to avoid numerical problems. The filtering step does not change the results. The second and third profiles presented are typical profiles from the ELFIE laser system for a 560 and 80 ps laser pulses, respectively. The profiles have been fitted with two Gaussian according to the following equations:

$$I(t)_{560\mathrm{ps}} = \exp\left(-\left(\frac{t}{0.337}\right)^2\right), \tag{3}$$

and

$$I(t)_{80ps} = \exp\left(-\left(\frac{t}{51.887}\right)^2\right). \tag{4}$$

The laser energy was measured systematically using a calorimeter calibrated at the start of the experiment and located in a leak behind the last mirror in the beam path. The laser spot diameter D was adapted by varying the focal distance for the ELFIE shots ($D = 4.6$ and 5.5 mm), while the LULI2000 shots ($D = 0.9$ mm) were realized with a random phase plate to obtain a homogeneous energy distribution.

The different parameters used in the different laser platforms are given in Table I.

B. Experimental impulse measurement

To measure the momentum coupling developed by a laser pulse, the classical experiment consists in applying a laser shot to a target mounted on a pendulum. The total momentum imparted to the target is then calculated from the measurement of the deflection of the pendulum in relation to the parameters of the pendulum. Usually either torsion[24,26] or ballistic[27,28] pendulums are used. In this case, the impulse imparted to the ballistic pendulum was calculated using the following relationship:

$$Q_{deflection} = \sqrt{2g\,M\,M_{eff}\,R_G(1-\cos(\theta_{\max}))}, \tag{5}$$

where Q is the momentum in N s, g is the standard gravity, M is the mass of the pendulum and sample assembly in kg, M_{eff} is the effective mass in kg, R_G is the radius of the center of gravity (distance between fulcrum and center of gravity, obtained via a CAD software), and $\theta_{\max}$ is the maximum deflection angle of the pendulum. The deflection angle is obtained by aiming a probe laser at the back of the pendulum with a mirror and recording the maximum angle reflected during the impact with a camera; the angle obtained is equal to twice the deflection angle θ. The effective mass is defined by

$$M_{eff} = \frac{I_n}{R_{eff}^2}, \tag{6}$$

where I_n is the total moment of inertia of the system (obtained via CAD) and R_{eff} is the distance between the fulcrum and the laser impact point.

In addition to the pendulum deflection method, PDV[29,30] measurements were also carried out. The measurement is based on interferometry. A probe continuous wave laser is focused on the pendulum and both the incident and reflected light are collected. This results in a beat signal, which is then recorded and analyzed using a sliding Fourier transform to extract a velocity profile as a function of time. The data obtained on the particle velocity of shock as a function of time are related to the shock pulse by the following equation:

$$Q_{PDV} = v_{PDV}\,M_{eff}\,\frac{R_{eff}}{R_{PDV}}, \tag{7}$$

where v_{PDV} is the maximum velocity of the profile (m/s) and R_{PDV} is the distance from the fulcrum to the PDV probe impact point in

TABLE I. Different laser parameters used for the shots on the ELFIE2018, LULI2020, and LULI2021 campaigns.

	λ (nm)	E (J)	$I\lambda\sqrt{\tau}$ (W/m s$^{1/2}$)	τ (ns)	ø (mm)
ELFIE2018	1057	0.29 to 11.43	2.00×10^3 to 8.13×10^4	0.08	4.6
ELFIE2018	1057	0.46 to 43.99	8.70×10^2 to 8.27×10^4	0.56	5.5
ELFIE2018	528	2.13 to 12.97	2.00×10^3 to 1.22×10^4	0.56	5.5
LULI2020/2021	1053	122.5 to 793.6	1.37×10^6 to 9.11×10^6	15	0.9

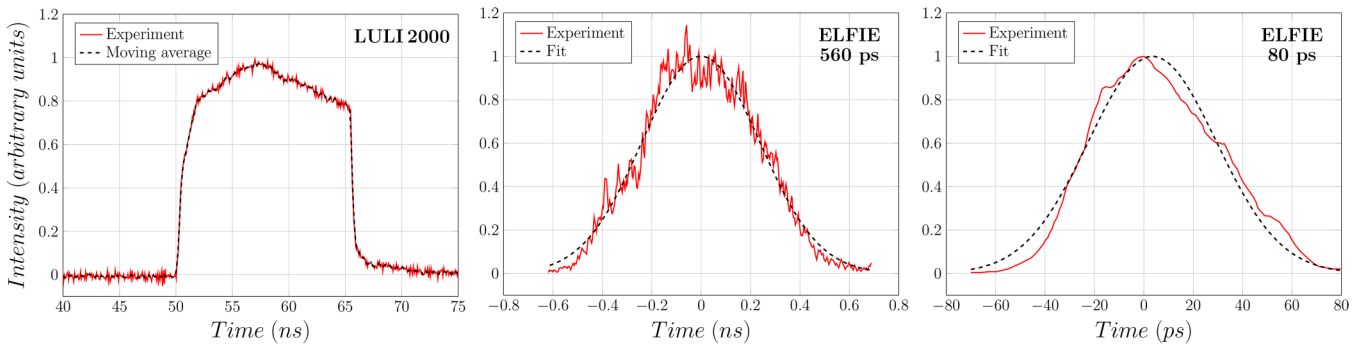

FIG. 1. Temporal pulse profile for the LULI2000 and ELFIE lasers. The intensity is in arbitrary units and the time in nanoseconds.

m. An example of a velocity profile obtained from a shot on an aluminum target at 661 J is given in Fig. 2.

The velocity profile shown in the figure is representative of the rest of the profiles obtained during the experiments, independent of the material. The PDV setup only allowed to measure the absolute value of velocity. Thus, only positive values are shown here. The main oscillation of ≈7.6 ms corresponds to the period of the pendulum while a second, smaller oscillation with a period of ≈60 μs can be observed all along the time axis. This oscillation corresponds to a mode of vibration of the pendulum assembly and the signal decreases with time. The main oscillation also exhibits a very slight damping of its motion with time passing, showing that our setup does not induce significant friction between the pendulum mount and the fulcrum during oscillation.

C. Experimental setup

For each campaign (ELFIE2018, LULI2020, LULI2021), the weight of the pendulum was adjusted to ensure that the deflection was small so that it remained in the field of view of the camera. This choice was also made for two more reasons. First, if the deflection is too large, the measurement made with the probe laser reflected on the mirror will not be feasible. Second, most of the time the PDV laser probes are positioned to illuminate the back of the pendulum, resulting in the pendulum hitting the probe mount in the event of a large shock. An example of the pendulum and the global experimental setup is shown in Fig. 3. The pendulum consists of a mainframe with a notch at the bottom to hold a mirror on which the continuous wave laser is reflected. This reflected laser oscillation from the pendulum movement is recorded by a camera aiming at the wall on which the laser is visible. Above the mirror, two 3D-printed polymer plates and the associated support screws are used to mount the samples.

For the LULI2020 and LULI2021 campaigns, the samples were 8 mm (15 × 15 × 8 mm) thick blocks of different materials: aluminum 6061-T6, porous graphite (EDM3) from POCO, copper, and tin. The last one was supplied in 8 and 5 mm thicknesses. In order to separate the plasma and debris contributions to total momentum, some EDM3 samples (marked EDM3M) were coated with aluminum: for these samples, the plasma contribution is

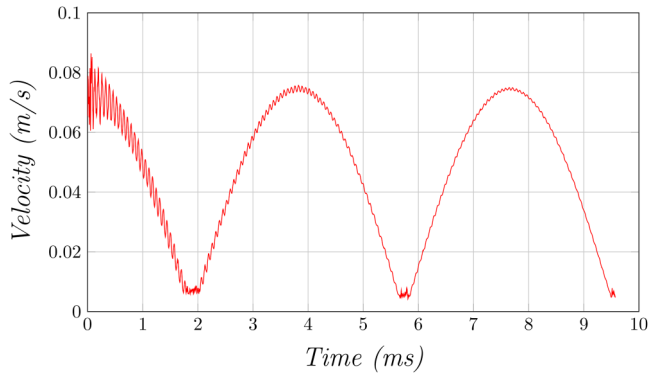

FIG. 2. Velocity depending on the time for a 661 J laser impulsion on an aluminum target mounted on a pendulum in a vacuum chamber.

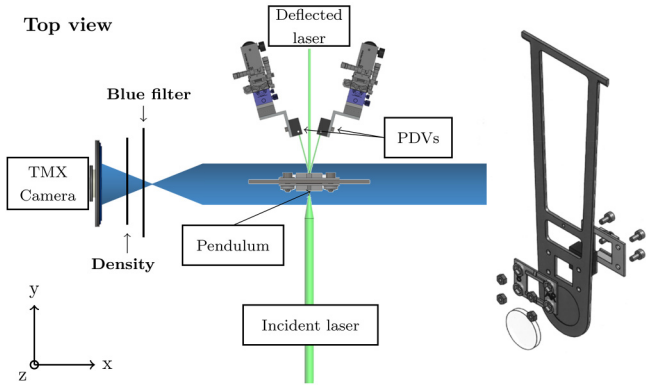

FIG. 3. Top view of the setup used during the ballistic pendulum experiments for the momentum calculation and exploded view of the pendulum assembly used for the experiments.

TABLE II. Summary of the targets thickness used for the ballistic pendulum experiments for each material studied.

	Materials					
Campaign	Aluminum	EDM3	EDM3M	Copper	Tin	Gold
ELFIE2018	100 μm	200 μm	…	…	…	300 μm
LULI2020	8 mm	8 mm	8 mm	8 mm	…	…
LULI2021	8 mm	8 mm	8 mm	8 mm	8 / 5 mm	…

expected to be the same as for bulk aluminum samples under similar irradiation conditions.

For the ELFIE2018 campaign, the materials studied were aluminum 99.99% (GoodFellow), EDM3, and gold. The laser energy on the target was much lower than for the LULI2020 and LULI2021 campaigns, so the targets chosen were thinner and lighter. The aluminum was 100 μm thick, while the EDM3 and gold had thicknesses of 200 and 300 μm, respectively. These differences were mainly due to machining limitations depending on the material. All sample sizes data are summarized in Table II.

Perpendicular to the incident laser light, a high speed camera (Phantom TMX 7510, 76 000 fps) was coupled to a continuous wave laser to illuminate the area of interest in the shots and obtain images of the debris produced by the shock.

D. Simulation of the interaction

The simulations were performed with the ESTHER code, a mono-dimensional Lagrangian hydrocode that describes laser–matter interaction and shock propagation in targets over a wide range of laser intensities, pulse durations, and wavelengths. It was originally developed for modeling femtosecond laser–matter interactions,[31–33] but has since been used for multiple nanosecond laser–matter interactions over a wide range of intensities, and has demonstrated high agreement with experiments for laser intensities up to 500 GW/cm^2 in the direct regime.[25,34–36]

The code models the laser propagation through matter by solving the Helmholtz equation for each cell using the refractive index found in Palik's tables for the solid part, while the plasma part is calculated by the Lorentz plasma model.[37] The hydrodynamics of the cells is modeled by calculating the evolution of their position at each time step coupled with the resolution of the conservation equations of mass, momentum, and energy in finite volumes. For the simulations presented in this paper, the global hydrodynamic approach of the cell stack is represented by the Bushman–Lomonosov–Fortov (BLF) equation of state.[38,39] Finally, the mechanical aspect is considered with the Steinberg–Cochran–Guinan model,[40] while the damage is represented with the Johnson's fracture model.[41]

ESTHER simulations require some input from the experiments, namely, the laser wavelength, a temporal pulse profile obtained from a photodiode measurement of the shot and finally the laser fluence at the center of the laser spot $F(0)$ in J/m^2. To obtain a radial profile of the laser spot used for the fluence calculation, we used camera imaging of the different lasers and chains. From this, we extracted a curve representing the fluence as a function of radius $F(r)$, which was then fitted using superGaussian sums. The fits obtained for the north and south chains of the LULI2000 laser are, respectively,

$$\frac{F_{North}(r)}{F(0)} = 0.83\, e^{-\left(\frac{r}{435}\right)^{10}} + 0.11\, e^{-\left(\frac{r}{530}\right)^{4}} + 0.052\, e^{-\left(\frac{r}{1100}\right)^{9}} + 0.008\, e^{-\left(\frac{r}{1600}\right)^{6}}, \quad (8)$$

$$\frac{F_{South}(r)}{F(0)} = 0.92\, e^{-\left(\frac{r}{420}\right)^{10}} + 0.07\, e^{-\left(\frac{r}{1050}\right)^{8}} + 0.01\, e^{-\left(\frac{r}{1400}\right)^{6}}, \quad (9)$$

where F is the fluence in J/m^2 and r is the radius in μm. The fit and profiles are given in Fig. 4.

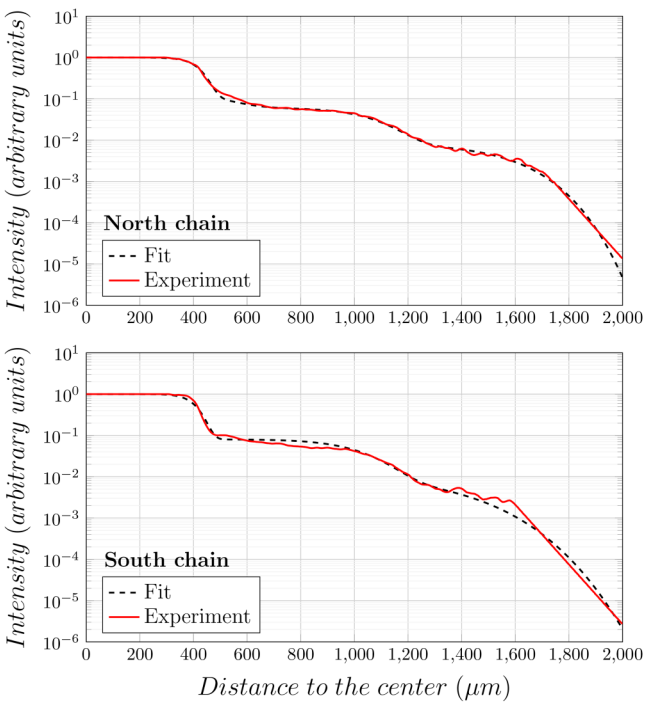

FIG. 4. Laser radial profile extracted from camera imaging measurement realized on the LULI2000 platform for the north and south chains with their associated fits.

For the ELFIE laser shots, the profiles were not measured experimentally, no DOE was used (diffractive optical element). The spot sizes used for these shots were 4.6 and 5.5 mm.

For a shot with an energy E in joules, the full 2D radial profile can be calculated as follows:

$$E = \int_0^\infty 2\pi r\, F(r)\, \mathrm{d}r = F(0)\, S, \tag{10}$$

where S is the effective area in m^2, defined as

$$S = \int \frac{F(r)}{F(0)}\, 2\pi r\, \mathrm{d}r. \tag{11}$$

Using Eqs. (8) and (9) in combination with Eq. (10), the fluence $F(0)$ was calculated for each shot for the three experimental campaigns.

E. Momentum computation

Because of momentum conservation, in the absence of any external force, the impulse of the whole system remains equal to zero. Thus, in order to extract from the simulation the total impulse $\mathcal{I}_{tot}$ imparted to the target, the following relationship is used:

$$\mathcal{I}_{tot} = \sum m_i\, v_i\,|_{v<0}, \tag{12}$$

where m_i is the mass per unit area of each cell and v_i is the material velocity in each cell. Only the cells with a negative velocity are taken into account, as the cells with a positive velocity represent matter ejected in the opposite direction, i.e., toward the laser. The resulting momentum is then calculated by applying this impulse to the effective area S given by Eq. (11),

$$Q_{tot} = \mathcal{I}_{tot}\, S. \tag{13}$$

Using this method, it is thus possible to extract the total momentum Q_{tot}, in which no distinction is made between the plasma and debris contributions, which we can directly compared to the pendulum measurements.

III. EXPERIMENTAL RESULTS

A. Momentum and momentum coupling results on aluminum

The experimental results are presented first, only for the aluminum samples, as this is the material with the best known properties and for which we have carried out the most experiments. Figure 5(a) shows the momentum calculated from Eqs. (5) and (7) for the laser shots on aluminum with energies ranging from 0.3 to 794 J. The mean deviation between the results of the two methods is 5.7% scattered over 20 shots (6.1% if all materials are considered for a total of 44 shots). The measurement uncertainties were estimated to be 5% for the laser energy and 10% for the momentum due to the deviation observed with the two measurement methods. The confrontation of the two methods described in Sec. II B

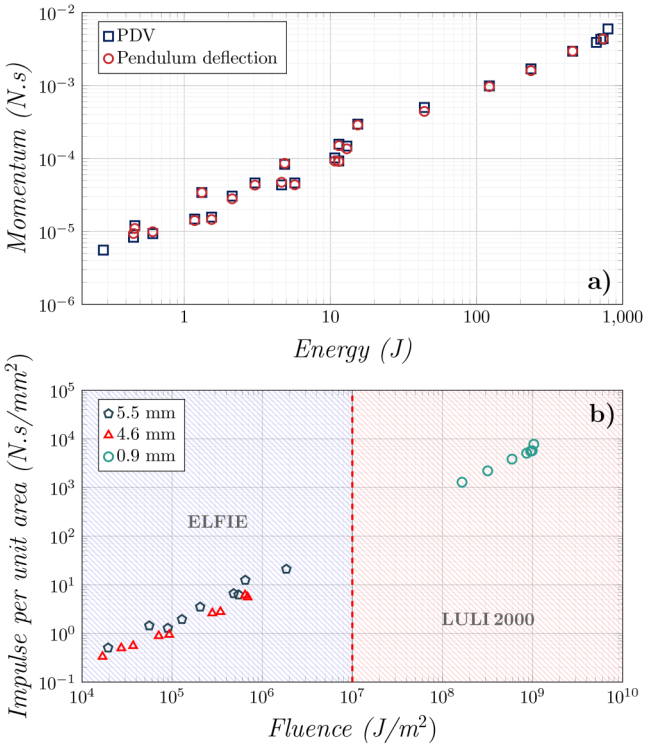

FIG. 5. (a) Momentum Q depending on the laser energy E for the shots on aluminum targets. The results are given for the PDV and the pendulum deflection calculation methods. The results come from the ELFIE2018, LULI2020, and LULI2021 campaigns. The uncertainties are estimated to be 5% for the laser energy and 10% for the momentum. (b) Impulse per unit area depending on the laser fluence for the shots on aluminum targets, only the PDV results are presented and separated depending on the laser spot size used during the experiments.

provides accurate results and confirms their validity and stability. A dependence of the momentum on the laser energy to the power of 0.85 is observed, which means that one could easily extrapolate the momentum for any given laser energy from these data, as long as the laser parameters put the interaction in the plasma regime according to the relation

$$Q = 2 \times 10^{-5}\, E^{0.85}. \tag{14}$$

For the sake of clarity, it has been decided to present only the PDV results in the following figures, as the results between the two methods are extremely close and it was the technique for which the most data were available.

Figure 5(b) presents the results on aluminum targets from PDV measurements. The results are presented as the impulse per unit are in $\mathrm{N\,s\,mm^{-2}}$ depending on the laser fluence ($F = E/S$, in $\mathrm{J/m^2}$) in order to take into account the potential effects induced by the different laser spot sizes used during the experiments. Indeed, as seen in the low fluence part of the figure, the use of a

5.5 mm laser spot size yields a slightly higher impulse per unit area than using a smaller 4.6 mm one. The results were arbitrarily separated at 10^7 J/m^2 to separate the campaigns performed on the ELFIE and LULI2000 laser platforms due to their different laser configurations. This separation was also applied for figures presented after. Multiple other phenomena can influence the momentum imparted to the targets when exposed to a laser irradiation. Optical properties of the materials, for instance, should play an important role in the results. Indeed, according to Palik's tables on optical constants,[42] the matter under laser irradiation should absorb more energy at 1053 or 1057 nm than at 532 nm. Conversely, if the interaction is in the plasma regime, the laser irradiation does not reach the surface of the matter anymore since it is then absorbed in the plasma. In this case, the plasma temperature is favored by higher wavelengths while the electron density increases with lower ones due to more mass ablated at the surface of the material.[43]

Preliminary simulations were performed and showed that all of our experiments except one were in the plasma regime of Phipps' model. The lowest energy shot (0.3 J, 1.7×10^4 J m^{-2}, $I\lambda\sqrt{\tau} \approx 10^3$ W/m s$^{1/2}$) only undergoes vaporization and was thus removed from the power fits related to the plasma regime realized in the rest of this work. Nonetheless, it is important to note that low energy shots reaching the plasma regime might not be doing so soon enough during the laser irradiation and could be, as a result, influenced by the relevant optical parameters from the vaporization and/or plasma regimes at the same time. However, a complete analysis on the influence of the optical parameters is outside the scope of this paper.

The comparison with Phipps' model,[20] considering only its plasma regime, was performed using the following equation:

$$C_{m_{plasma}} = 184 \frac{\Psi^{9/16}}{A^{1/8}(I\lambda\sqrt{\tau})^{1/4}} \quad (N/MW). \tag{15}$$

With Ψ being equal to

$$\Psi = \frac{A}{2[Z^2(Z+1)]^{1/3}}, \tag{16}$$

where A is the average atomic mass number and Z is the average ionization state in the plasma. The model described in Phipps' paper calculates Z at each time step through Saha's equation.[44] Calculations have been carried out for ($2 \leq Z \leq 7$), which cover all experimental results. The use of Eq. (15) thus gives us a range of possible momentum couplings for a set of laser parameters. The experimental momentum coupling was also extracted from each experimental point using the results from Fig. 5 and Eq. (2).

Figure 6 shows the momentum coupling of the aluminum shots as a function of $I\lambda\sqrt{\tau}$. Each color represents a specific set of laser parameters (λ, τ, E, ø), three sets of laser parameters are presented using the ELFIE laser platform while one set is presented using the LULI2000 one. The shots performed with the latter follow a power law while the shots of the ELFIE platform show more dispersion, even with the same set of laser parameters. A separation can be seen between 10^5 and 10^6 W/m s$^{1/2}$ corresponding to the

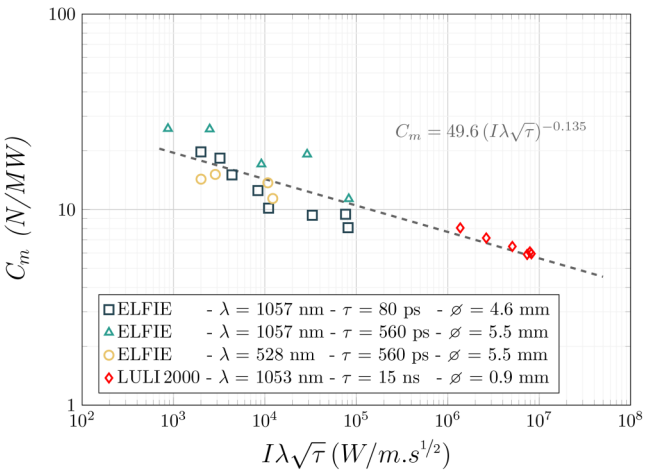

FIG. 6. Momentum coupling (N/MW) depending on $I\lambda\sqrt{\tau}$ calculated for each experimental campaign conducted on aluminum targets. Each set of laser parameters is separated for better visualization. The overall fit is shown as a dashed line.

range of $I\lambda\sqrt{\tau}$ covered by each platform (the shots on the ELFIE platform range from 8.70×10^2 to 8.27×10^4 W/m s$^{1/2}$ while the LULI2000 ones range from 1.37×10^6 to 9.11×10^6 W/m s$^{1/2}$. Overall, all the experimental results give a momentum coupling coefficient following a power law with a −0.135 factor.

The data shown in Fig. 7 represent the experimental results compared to the literature[21,22,24] and the simplified Phipps' model [Eq. (15)], for which the predicted momentum coupling range is

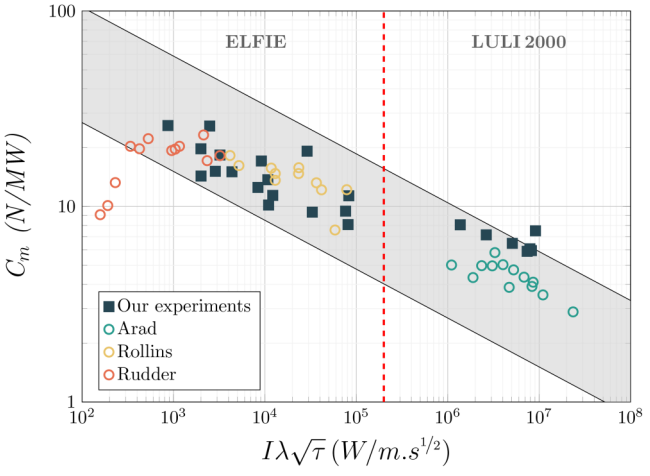

FIG. 7. Momentum coupling (N/MW) depending on $I\lambda\sqrt{\tau}$ calculated for each experimental campaign conducted on aluminum targets compared to Phipps' simplified model and other experimental results from Rudder,[21] Arad,[24] and Rollins.[22]

represented by the gray band for the following parameters: $2 \leq Z \leq 7$. Almost every experimental point from the literature is within the range described, except for some from Rudder's experiments which show a configuration that reaches the vapor regime threshold at low $I\lambda\sqrt{\tau}$, a regime not considered in the simplified model we used (Sec. III B).

Our experimental results can be divided into two parts with a threshold around $I\lambda\sqrt{\tau} = 10^5\ W/m\,s^{\frac{1}{2}}$. Our data at higher $I\lambda\sqrt{\tau}$ are extremely close to one another and follow a trend line except for one point, which is slightly higher and corresponds to the only shot of the LULI2021 campaign on aluminum. These results also follow the same slope as those obtained using Eq. (15). It is also interesting to note that there is a slight difference between our results and those observed in Arad's work.[24] These differences might be attributed to the different experimental setups used. Indeed, in their work, two torsion pendula are used, which could induce more deviation from their results. The configuration of Arad *et al.* also uses a pulse duration of 500 ps and a 200 μm laser spot size, while our results for an equivalent $I\lambda\sqrt{\tau}$ use a 15 ns pulse duration and a 900 μm. The differences in both the setups and measurement methods, coupled with the deviation measured in our experimental work could very well bridge the gap between our and Arad's *et al.* datasets. At the same time, the use of different pulse durations could also result in differences in the momentum produced (see Fig. 8)

On the contrary, our data points below the threshold value $I\lambda\sqrt{\tau} \approx 10^5\ W/m\,s^{\frac{1}{2}}$ are in agreement with the literature. The observed dispersion is caused by the different pulse durations and wavelengths used in this range of $I\lambda\sqrt{\tau}$ as described in Sec. III B.

B. Laser parameters influence

Figure 8 shows the effect of pulse duration on the calculated momentum coupling imparted to a target by a laser shock at different energies as a function of $I\lambda\sqrt{\tau}$. There is a clear divide between shots at 80 and 560 ps, the latter producing on average 87% more momentum over the range considered. This seems to be the explanation for the dispersion observed in the shots below $I\lambda\sqrt{\tau} \approx 10^5$ W/m s$^{\frac{1}{2}}$.

The same type of comparison was made to detect a possible wavelength influence on the momentum for shots with a 560 ps pulse duration and a 5.5 mm laser spot diameter (see Fig. 9).

The two wavelengths investigated were 1057 and 528 nm. The influence of the wavelength on the momentum coupling appears to be modest, similar to the effect of the pulse duration. The limited number of experimental points for the two configurations reduces the accuracy of the evaluation of the wavelength effect on the momentum coupling over wider ranges of $I\lambda\sqrt{\tau}$, but the mean deviation observed between the two wavelengths for the $10^3 < I\lambda\sqrt{\tau} < 10^4$ W/m s$^{\frac{1}{2}}$ range is $\approx$35%. These results might also be influenced by the low energy of the pulses, which places them close to the transition of the vaporization/plasma regime, thus involving multiple, potentially conflicting, optical, thermal, and mechanical phenomena.

It is also important to note that the wavelengths studied here are only a factor of two compared to the pulse durations which are a factor of 7, thus increasing their influence. Overall, it seems that the $I\lambda\sqrt{\tau}$ parameter, although currently the appropriate choice to describe the interaction, does not fully capture all the phenomena involved in the whole interaction that takes place to induce the momentum imparted by a laser shock. Still, knowing the influence of the wavelength and pulse duration, coupled with the effect of the laser spot size used given in Fig. 5(b), could benefit laser ablation propulsion for example. Using a low energy coupled with a long pulse duration and a infrared laser wavelength would allow to produce high momentum with an $I\lambda\sqrt{\tau}$ placing the interaction in the vaporization regime while limiting the matter ablation due to low energy and duration of the pulse.

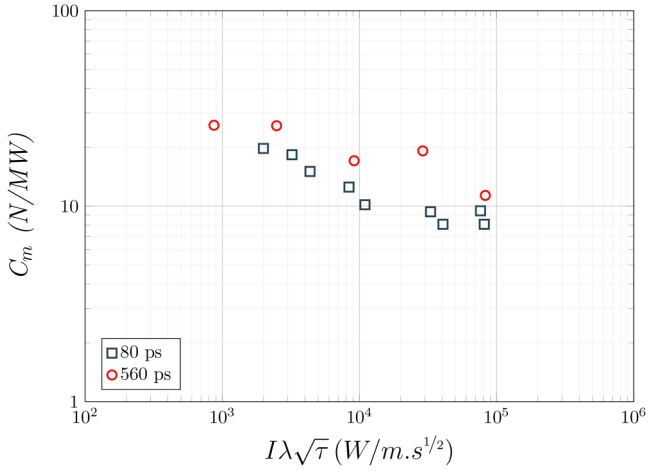

FIG. 8. Pulse duration influence on the momentum coupling. Shots from ELFIE2018 campaign for 560 and 80 ps pulses, spot sizes are, respectively, 4.6 and 5.5 mm.

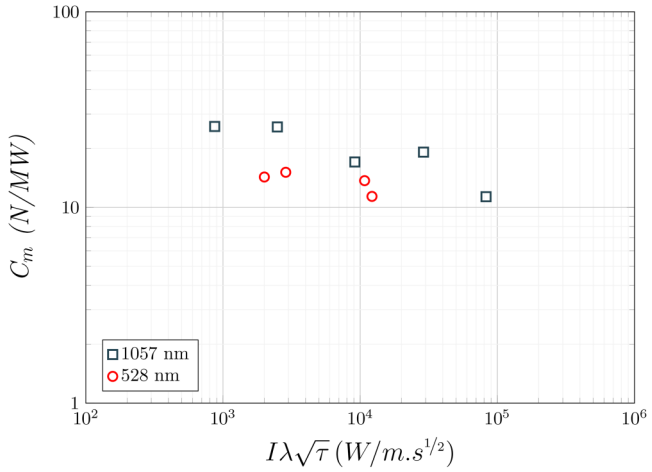

FIG. 9. Wavelength influence on the momentum coupling. Shots from ELFIE2018 campaign for a 560 ps pulse, spot size is 4.6 mm.

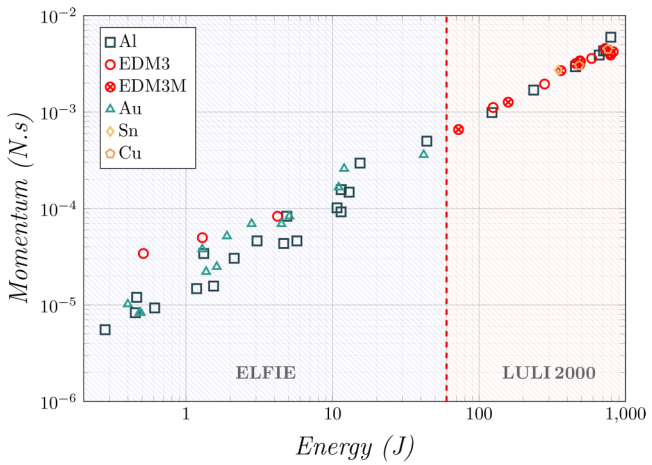

FIG. 10. Momentum depending on the energy for aluminum, carbon, gold, tin, and copper.

C. Target material influence

To complete the results using different laser parameters, the material influence was investigated with shots on carbon, aluminum-coated carbon, gold, tin, and copper targets. The results of the momentum and momentum coupling calculations are shown in Figs. 10 and 11. Table III shows all the data from the experiments on all the materials.

The influence of the material properties on the imparted momentum when subjected to laser irradiation in the plasma regime does not appear to be significant. In particular, the comparison of bulk aluminum and EDM3M, an aluminum-coated carbon, suggests that the influence of material properties is negligible. In fact, the use of an aluminum coating on the carbon sample ensures that the laser interaction at the surface and that the plasma is the same for both materials, which means that the mechanical loading imparting the momentum to the target should also be the same. Therefore, if the debris produced by the irradiated target contributed significantly to the total momentum, a strong difference would be observed between the two materials. This result will be confirmed by the discussion in Sec. III D.

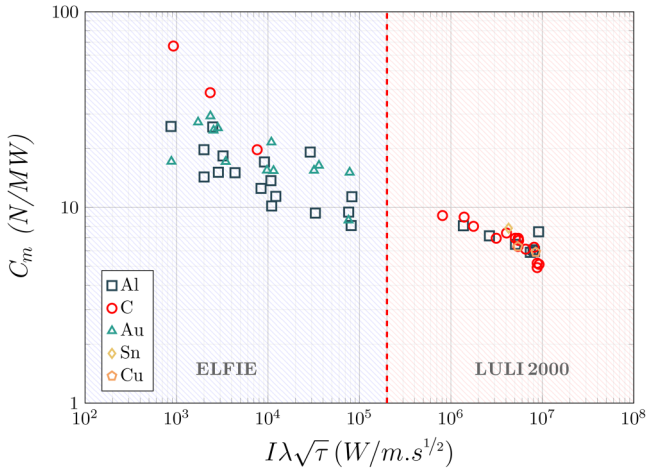

FIG. 11. Momentum coupling depending on $I\lambda\sqrt{\tau}$ for aluminum, carbon, gold, tin, and copper.

Moreover, no differences were observed between the two types of carbon samples, meaning that the optical properties of the surface irradiated also do not influence the resulting momentum imparted to the target as long as the interaction is in the plasma regime. As a result, the two types of carbon samples have been grouped together under the name "Carbon" in the plots presented after. However, for low $I\lambda\sqrt{\tau}$ ($\approx 10^3$ W/m s$^{\frac{1}{2}}$), a difference is observed in the momentum coupling of carbon and of the other materials. A significantly higher value is observed for EDM3 samples.

Multiple material properties can explain these differences between carbon and metal samples. The specific heat of carbon is lower than for metals while their optical absorption is much lower before reaching their melting temperature. Once reached, it quickly catches up to typical carbon values.[45] EDM3 due to its carbonaceous nature also presents a higher enthalpy of vaporization compared to aluminum or copper [$\Delta_{f_C} H^0(0\,\mathrm{K}) = 711.19 \pm 0.46$ kJ/mol, $\Delta_{f_{Al}} H^0(0\,\mathrm{K}) = 327.3 \pm 4.2$ kJ/mol, $\Delta_{f_{Cu}} H^0(0\,\mathrm{K}) = 336.4 \pm 1.2$ kJ/mol].[46]

Although all these material properties influence one another, it seems that carbon requires more energy to reach its plasma phase, causing the plasma regime threshold to be reached at higher $I\lambda\sqrt{\tau}$ values for EDM3 compared to the other metallic materials studied. More information on this can be found in the work of Sinko *et al.*[47] The effects of pulse duration and wavelength were also observed for gold in the $I\lambda\sqrt{\tau} < 10^5$ W/m s$^{\frac{1}{2}}$ part, but the data were too sparse to make the same observation for the other materials studied. On the other hand, the part above 10^5 W/m s$^{\frac{1}{2}}$ followed a straight line for all materials.

D. Crater analysis

As mentioned in the introduction, there are two contributions to the momentum. The plasma part and the debris (solid and/or liquid) result from the mechanical effect of the shock wave in the sample. Their addition is equal to the total momentum transferred to the pendulum during the experiments. To study this mechanical contribution, we first considered the craters formed after the shock. Figure 12 shows the volume of the crater as a function of the laser energy. This volume was obtained with an optical profilometer and a power dependence with the laser energy of the shots was observed for all materials. The copper samples show a particular behavior compared to aluminum and carbon, but the lack of samples does not give enough information to extrapolate a particular trend. The carbon samples show crater volumes that are on average 10 times larger than those observed for the aluminum samples, while leading to similar momentum couplings (cf. Fig. 10). These results suggest that the contribution of the ejecta to the momentum during laser shock is negligible. The slope of the plots varies from one material to

TABLE III. Data used for this study

		E	I	λ	τ	ø	Q_{PDV}	Q_{Def}	Q_{Sim}	$C_{m_{PDV}}$	$C_{m_{Def}}$	$C_{m_{Sim}}$
Material	Campaign	J	GW/cm^2	nm	ns	mm		N.s			N/MW	
Al	ELFIE2018	11.43	859.5	1057	0.08	4.6	9.235E-5	9.099E-5	1.134E-4	8.08	7.96	9.93
Al	ELFIE2018	1.54	116.1	1057	0.08	4.6	1.570E-5	1.455E-5	2.022E-5	10.17	9.43	13.10
Al	ELFIE2018	4.64	349.0	1057	0.08	4.6	4.340E-5	4.716E-5	5.311E-5	9.36	10.17	11.45
Al	ELFIE2018	10.73	807.2	1057	0.08	4.6	1.015E-4	9.246E-5	1.056E-4	9.47	8.62	9.84
Al	ELFIE2018	1.18	88.8	1057	0.08	4.6	1.477E-5	1.408E-5	1.610E-5	12.52	11.93	13.64
Al	ELFIE2018	0.61	46.2	1057	0.08	4.6	9.235E-6	9.899E-6	9.306E-6	15.05	16.13	15.17
Al	ELFIE2018	0.28	21.1	1057	0.08	4.6	5.541E-6		4.122E-6	19.74		14.68
Al	ELFIE2018	0.45	34.1	1057	0.08	4.6	8.311E-6	9.358E-6	7.911E-6	18.33	20.64	17.45
Al	ELFIE2018	15.40	115.8	1057	0.56	5.5	2.955E-4	2.873E-4	1.641E-4	19.18	18.65	10.65
Al	ELFIE2018	43.99	330.7	1057	0.56	5.5	4.991E-4	4.409E-4	4.02E-4	11.35	10.02	9.13
Al	ELFIE2018	4.87	36.6	1057	0.56	5.5	8.312E-5	8.566E-5	6.220E-5	17.08	17.60	12.78
Al	ELFIE2018	1.32	10.0	1057	0.56	5.5	3.417E-5	3.400E-5	2.347E-5	25.80	25.67	17.72
Al	ELFIE2018	0.46	3.5	1057	0.56	5.5	1.201E-5	1.098E-5		25.94	23.73	
Al	ELFIE2018	11.45	86.1	528.5	0.56	5.5	1.570E-4	1.497E-4	1.605E-4	13.71	13.07	14.02
Al	ELFIE2018	12.97	97.5	528.5	0.56	5.5	1.478E-4	1.353E-4	1.741E-4	11.39	10.43	13.42
Al	ELFIE2018	3.05	22.9	528.5	0.56	5.5	4.618E-5	4.312E-5	7.336E-5	15.13	14.13	24.04
Al	ELFIE2018	2.13	16.0	528.5	0.56	5.5	3.048E-5	2.798E-5	5.809E-5	14.31	13.14	27.28
Al	LULI2020	708.20	6142.0	1053	15	0.9	4.303E-3		1.960E-3	6.08		2.77
Al	LULI2020	660.90	5731.8	1053	15	0.9	3.898E-3		1.788E-3	5.90		2.71
Al	LULI2020	735.70	6380.5	1053	15	0.9	4.376E-3	4.348E-3	2.046E-3	5.95	5.91	2.78
Al	LULI2020	454.80	3944.3	1053	15	0.9	2.947E-3	2.954E-3	1.239E-3	6.48	6.50	2.72
Al	LULI2020	122.50	1062.4	1053	15	0.9	9.874E-4	9.645E-4	4.196E-4	8.06	7.88	3.43
Al	LULI2020	235.90	2045.9	1053	15	0.9	1.689E-3	1.599E-3	7.099E-4	7.16	6.78	3.01
Al	LULI2021	793.63	7194.7	1053	15	0.9	5.960E-3		2.157E-3	7.51		2.72
EDM3	ELFIE2018	45.08	316.2	1057	0.56	5.5		1.238E-4			2.75	
EDM3	ELFIE2018	4.21	29.5	1057	0.56	5.5	8.312E-5	9.095E-5		19.73	21.59	
EDM3	ELFIE2018	1.29	9.1	1057	0.56	5.5	4.987E-5	4.661E-5		38.62	36.10	
EDM3	ELFIE2018	0.51	3.6	1057	0.56	5.5	3.417E-5	3.104E-5		66.86	60.73	
EDM3	LULI2020	587.00	5090.9	1053	15	0.9	3.594E-3	3.480E-3		6.12	5.93	
EDM3	LULI2020	280.10	2429.2	1053	15	0.9	1.949E-3	1.726E-3		6.96	6.16	
EDM3	LULI2020	124.80	1082.4	1053	15	0.9	1.114E-3	1.016E-3		8.92	8.14	
EDM3	LULI2020	484.70	4203.6	1053	15	0.9	3.063E-3	3.051E-3		6.32	6.30	
EDM3	LULI2021	790.38	6760.1	1053	15	0.9	3.893E-3			4.93		
EDM3M	LULI2021	823.90	7145.4	1053	15	0.9	4.215E-3			5.12		
EDM3M	LULI2021	456.81	3901.9	1053	15	0.9	3.180E-3			6.96		
EDM3M	LULI2021	786.19	6804.8	1053	15	0.9	4.079E-3			5.19	5.06	
EDM3M	LULI2020	727.70	6311.1	1053	15	0.9	4.556E-3	4.583E-3		6.26	6.30	
EDM3M	LULI2020	362.50	3143.8	1053	15	0.9	2.683E-3	2.694E-3		7.40	7.43	
EDM3M	LULI2020	492.40	4270.4	1053	15	0.9	3.341E-3	3.132E-3		6.79	6.36	
EDM3M	LULI2020	72.40	627.9	1053	15	0.9	6.581E-4	5.935E-4		9.09	8.20	
EDM3M	LULI2020	158.10	1371.1	1053	15	0.9	1.266E-3			8.01		
EDM3M	LULI2020	487.80	4230.5	1053	15	0.9	3.392E-3	3.266E-3		6.95	6.70	
Au	ELFIE2018	5.07	381.42	1057	0.08	4.6	8.313E-5	8.655E-5		16.39	17.07	
Au	ELFIE2018	11.00	827.71	1057	0.08	4.6	1.663E-4	1.787E-4		15.11	16.24	
Au	ELFIE2018	1.62	121.78	1057	0.08	4.6	2.494E-5	2.654E-5		15.40	16.39	
Au	ELFIE2018	4.48	337.05	1057	0.08	4.6	6.928E-5	7.372E-5		15.46	16.45	
Au	ELFIE2018	1.37	103.24	1057	0.08	4.6	2.125E-5	2.294E-5		15.48	16.71	
Au	ELFIE2018	0.49	36.48	1057	0.08	4.6	8.313E-6	9.436E-6		17.14	19.46	
Au	ELFIE2018	0.40	29.99	1057	0.08	4.6	1.016E-5			25.48		
Au	ELFIE2018	12.28	86.17	1057	0.6	5.5		3.201E-4			26.06	
Au	ELFIE2018	41.89	293.84	1057	0.6	5.5	3.602E-4	3.360E-4		8.60	8.02	

TABLE III. (*Continued.*)

		E	I	λ	τ	ø	Q_{PDV}	Q_{Def}	Q_{Sim}	$C_{m_{PDV}}$	$C_{m_{Def}}$	$C_{m_{Sim}}$
Material	Campaign	J	GW/cm^2	nm	ns	mm		N.s			N/MW	
Au	ELFIE2018	4.20	29.47	1057	0.6	5.5		1.176E-4			28.00	
Au	ELFIE2018	1.29	9.07	1057	0.6	5.5	3.787E-5	3.782E-5		29.31	29.26	
Au	ELFIE2018	0.48	3.39	1057	0.6	5.5	8.313E-6	7.641E-6		17.18	15.79	
Au	ELFIE2018	12.00	84.18	528.5	0.6	5.5	2.586E-4	2.349E-4		21.55	19.58	
Au	ELFIE2018	2.80	19.62	528.5	0.6	5.5	6.928E-5	6.184E-5		24.77	22.11	
Au	ELFIE2018	1.90	13.30	528.5	0.6	5.5	5.173E-5	5.058E-5		27.29	26.68	
Sn	LULI2021	347.73	3633.4	1053	15	0.9	2.724E-3			7.83		
Cu	LULI2021	757.51	6570.0	1053	15	0.9	4.476E-3			5.91		
Cu	LULI2020	482.60	4185.4	1053	15	0.9	3.044E-3			6.31		

another with $V_{crat_C} \propto E^{0.85}$ for carbon and $V_{crat_{Al}} \propto E^{1.19}$ for aluminum. However, the fit quality was a lot better for aluminum than for carbon samples, for which a large dispersion is observed, probably due to some randomness in the brittle failure process.

To further understand the different effects that take place in the cratering of the different materials studied, surface imaging of the shot samples was performed on post-mortem samples, the resulting images are shown in Fig. 13. The different metallic targets show similar crater shapes, except for the tin sample where a crown of liquid projected matter is observed in addition to the laser spot sized initial crater. This observation is supported by the low melting point of tin (231.9 °C) compared to the other materials in the study. Significant differences are observed between the craters of metallic and carbon targets, with the latter showing significantly larger craters. These craters are composed of large chunks of material that have been partially detached from the bulk material, but not completely separated from it, and therefore did not participate in the ejection momentum. This observation supports the dispersion of the results observed in the volume of the craters produced in the different carbon samples compared to the aluminum samples, which show a clearer trend.

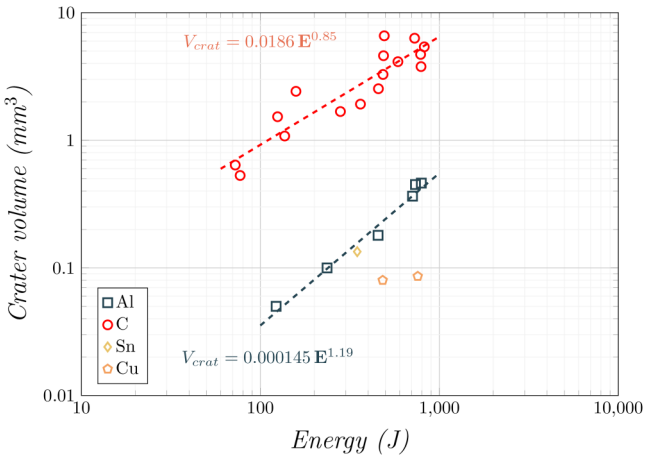

FIG. 12. Crater volume (mm^3) depending on the laser energy (J) for aluminum, carbon, tin, and copper.

It is also interesting to note that the power law dependency of the crater volume to the laser energy follows the same trend as the one observed between the crater volume and kinetic energy in the case of classical hypervelocity impacts.[48] Taking into account the theory of Pirri[7] linking laser parameters to an equivalent projectile for hypervelocity impact, these results could also serve for more classical HVI studies.

To complete the experimental study of the ejecta, shadowgraphy was performed during the shots to observe the ejection of debris for the different materials.

In Fig. 14, camera acquisitions during the ejection debris process are displayed for aluminum, carbon, and tin samples. The plasma expansion was not shown due to the saturation of the camera caused by the plasma. The acquisitions were performed on time scale allowing the debris to travel along the horizontal frame of the camera. The three materials were chosen for their different modes of matter ejection. In the case of aluminum, the ejection cloud appears to be the fastest out of the studied materials and displays the smallest fragments. The matter takes the form of an ejection cone quite early (15.41 μs) while at a later time, some fragments seem to form "filaments." In the case of the carbon images, the opposite is observed: most of the mass ejected does so in the form of large debris with a low velocity and an irregular shape, typical of brittle materials. Moreover, numerous smaller fragments are also visible, with roughly the same velocity. As regards tin, the images show debris having a similar velocity to that of carbon, but with a very different ejection pattern. The ejected matter is expelled from the crater in several filaments that break into fragments. Contrary to aluminum, these filament structures are clearly isolated from one another. Due to the low melting temperature of tin, it is supposed that all this ejection process occurs in the liquid state. The resulting fragments seem to be slightly larger than in the case of aluminum.

Even though the quality of the images can only lead to a qualitative analysis of the debris, their study highlights the widely different mode of material ejection after laser irradiation. Coupled with the results from Fig. 11, these observations strongly suggest

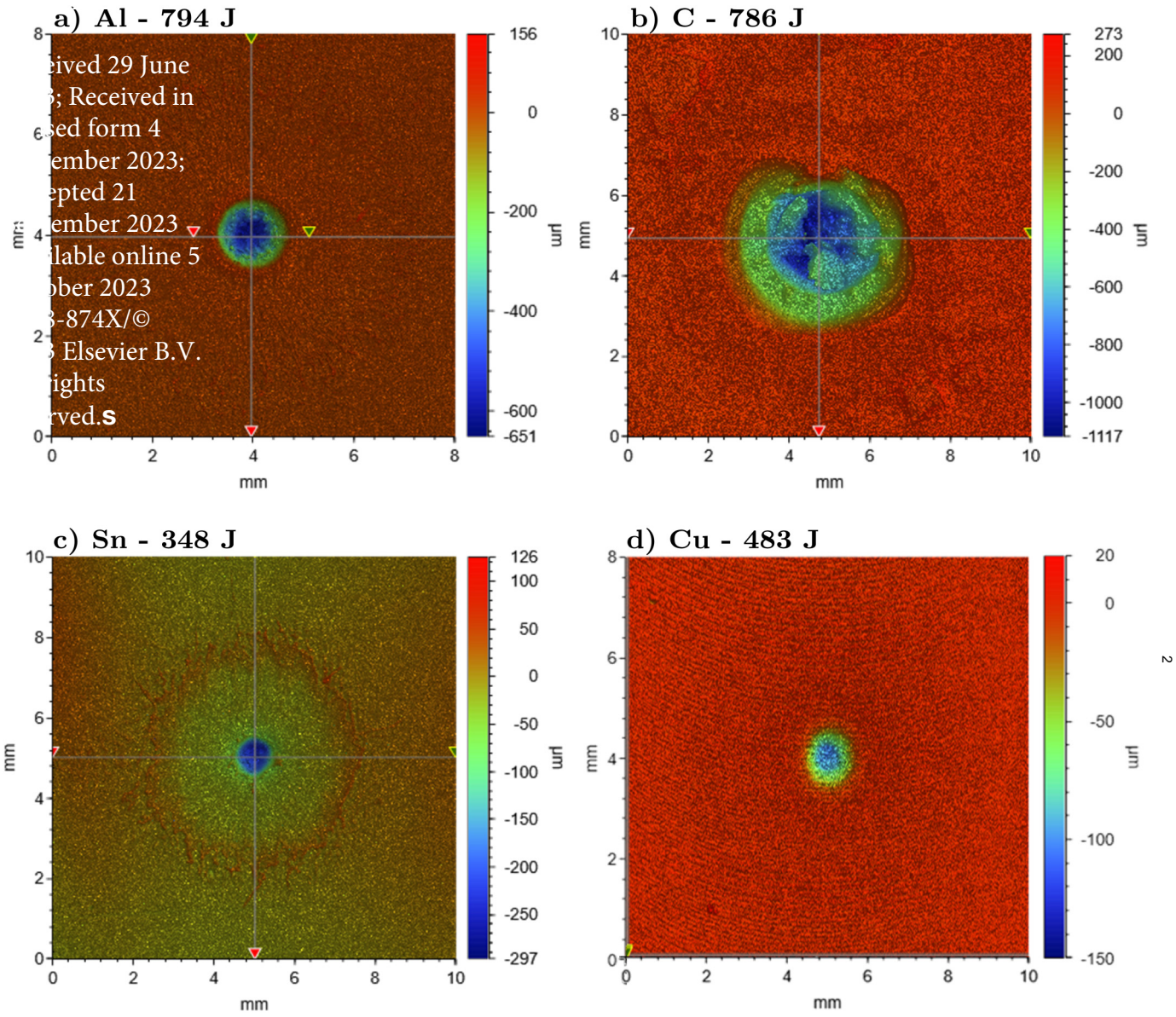

FIG. 13. Profilometer imaging of the crater for (a) aluminum, (b) carbon, (c) tin, and (d) copper for shots of the LULI2020 and LULI2021 campaigns.

that the carbon debris does not carry a large portion of the momentum in the laser configurations studied.

IV. SIMULATION RESULTS ON ALUMINUM

The laser–matter interaction simulations were performed with the mono-dimensional Lagrangian hydrocode ESTHER to calculate the momentum using the method described in Sec. II E. Figure 15 presents the results of the simulations using this method for aluminum targets. The mean deviation between ESTHER simulations and the experimental results is ≈35.1%.

Interestingly, the simulations of the shots from the ELFIE2018 campaign present a lower deviation compared to the experiments with an average of 27% while the simulations of the shots from the LULI2020 and LULI2021 campaigns present a mean deviation of 57% compared to the experimental results. This can be partly explained by the spot size used in the LULI2020 and 2021 that was 0.9 mm coupled with a long 15 ns pulse duration, which induced a

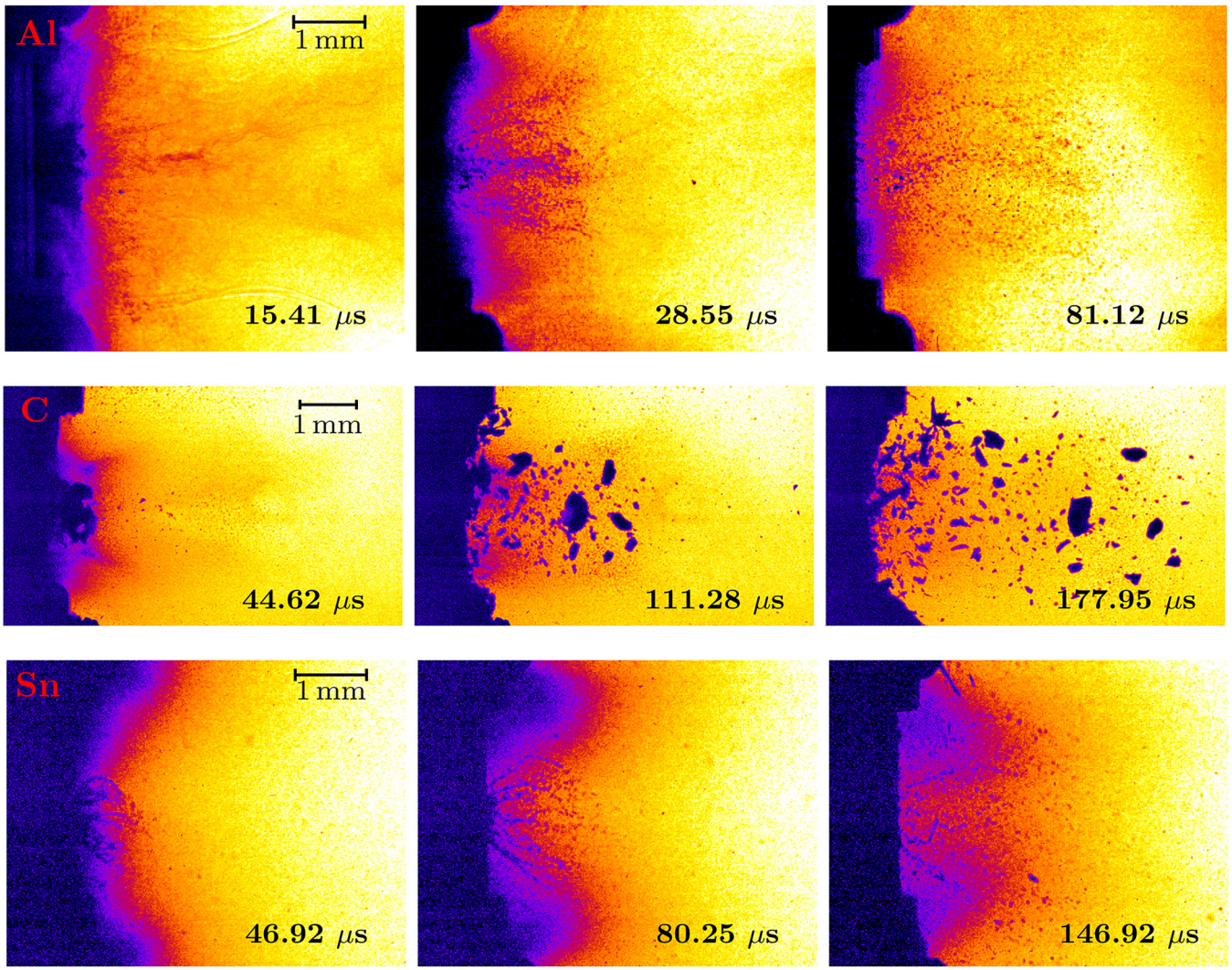

FIG. 14. Camera acquisition of the matter expelled from the target for Al, carbon, and Sn after laser shock on sample mounted on a pendulum.

stronger multidimensional release of the plasma that was not captured by the code.[49] The other materials were not simulated due to the lack of accurate models for those.

Above $I\lambda\sqrt{\tau} \approx 10^5$ W/m s$^{\frac{1}{2}}$ both the experimental and simulation results follow the same slope. In the $I\lambda\sqrt{\tau} < 10^5$ W/m s$^{\frac{1}{2}}$ range, the ELFIE2018 simulation and experiments present more dispersion. This can be explained by the different sets of laser parameters involved in this range of $I\lambda\sqrt{\tau}$.

Indeed, different laser spots (4.6 and 5.5 mm), pulse durations (80 and 560 ps), and wavelengths (1057 and 528 nm) are used and induce different influence of the edge effects. Moreover, the trend line of each set of laser parameters is well represented by the simulations, which gives us confidence in our simulation results. Thus, for one set of parameters, the simulation results do not show any significant dispersion and all follow a similar trend to that observed for the campaigns on the LULI2000 platform as shown in Fig. 15. Interestingly, the trends observed in Fig. 15(b) via simulation for the effect of pulse duration and wavelength are not the one observed in the experimental results from Figs. 8 and 9. In the simulations, there is no noticeable difference in the momentum coupling between the simulated shots with a pulse duration of 80 and 560 ps. Moreover, a wavelength effect is observed, but contrary to what was observed experimentally, a shorter wavelength induces a higher momentum coupling. These effects can either be a demonstration of the limitations of the code for the calculation of such phenomena or the result of the uncertainties associated with the experimental parameters on the pulse duration and laser pulse energy or a mix of both.

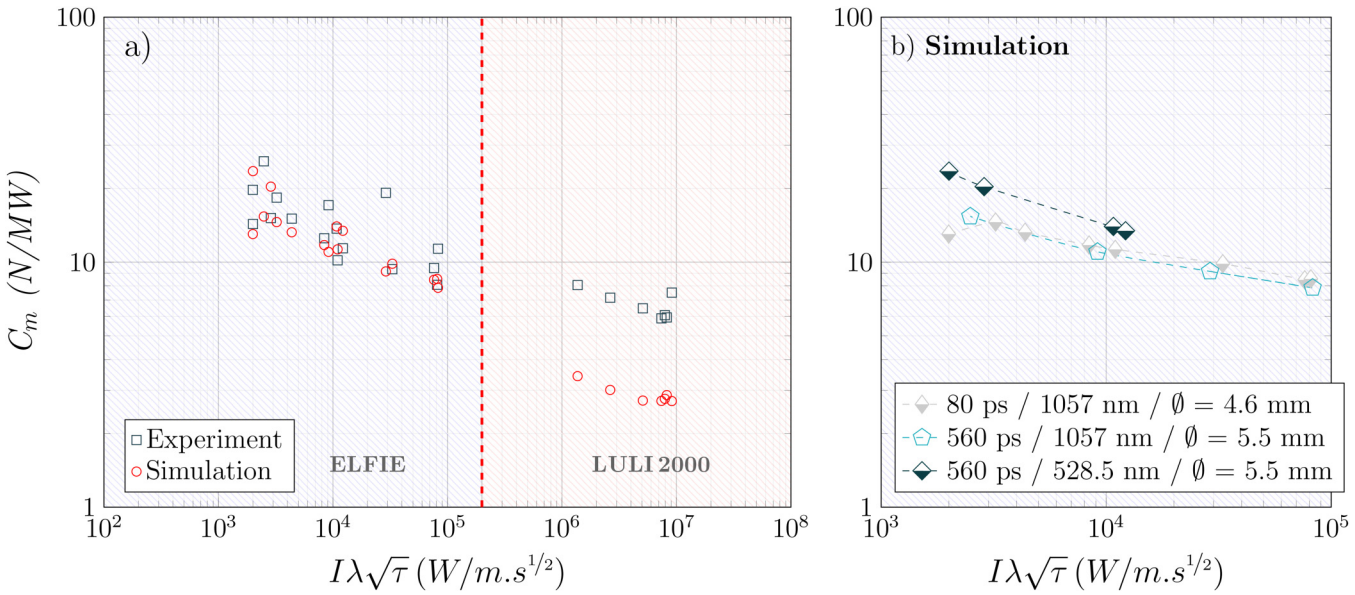

FIG. 15. (a) Momentum coupling depending on $I\lambda\sqrt{\tau}$ for the experimental and simulated results. (b) Focus on the simulation results of the ELFIE2018 campaign depending on the laser parameters.

V. CONCLUSION

In this study, we presented highly accurate results from ballistic pendulum experiments using laser shots on targets made of aluminum, carbon, gold, tin, or copper. The momentum and momentum coupling imparted to the targets were extracted using two diagnostics: PDV and pendulum deflection measurement. The results demonstrated the stability of our experiments with an average difference of ≈5.7% between the two methods for shots on aluminum and a global deviation of 6.1% if all the materials studied are taken into account, namely, aluminum, carbon, tin, gold, and copper, showing that the momentum measurement methods are efficient for all types of materials. The results were then compared with works from the literature as well as Phipps' simplified model and showed good agreement and stability. The wide range of laser parameters studied on similar laser platforms showed that the momentum coupling produced by a laser pulse for a given set of laser parameters can be predicted in a satisfactory manner. Parameters such as λ, τ and ø do have an influence although not significant in the range studied. This can be important in order to improve the LAP process, for example, by selecting parameters, in order to keep a high resulting momentum while decreasing the amount of ablated matter.

The comparison of the momentum imparted to multiple metallic and carbonaceous samples showed that the initial properties of the irradiated material had a negligible influence as long as the interaction was in the plasma regime. More specifically, the comparison of the aluminum and EDM3 samples, to which a small coating of aluminum was applied, allowed the same laser–matter interaction to be produced on both materials. Even though these materials had different modes of matter ejection, as well as different thermal and mechanical properties, the momentum imparted to them remained the same when subjected to laser irradiation. This result was also confirmed through the comparison between the EDM3 and aluminum-coated EDM3 samples which also exhibited the same properties, confirming the complete prevalence of the plasma effect in detriment to the material surface effect in the high energy range covered by the experiments performed on the LULI2000 platform.

Analysis of high-speed camera images allowed a qualitative analysis of the different mode of ejection of the matter after laser irradiation for aluminum, carbon, and tin. The observations hinted in the same direction as the momentum coupling measurement results, indicating that the debris produced by the experiments does not seem to impart a significant part of the momentum compared to the influence of the plasma expansion. The analysis of the crater volume depending on the laser energy showed a power dependence that could be used in the study of hypervelocity impacts for applications such as laser deorbiting but also for more classical hypervelocity impact applications were the kinetic energy is similarly linked by a power law to the crater volume.

To complement the study, mono-dimensional simulations of the momentum coupling were carried out for the three campaigns studied with aluminum targets using the Lagrangian code ESTHER. The results showed a global deviation of ≈35% from the experiments for all shots. The deviation observed for the two campaigns on the LULI2000 platform was ≈57%, while the one observed for the campaign on the ELFIE platform presented a global deviation of ≈27% although it covered a wide range of laser parameters. The differences between the LULI and ELFIE

campaigns can be mainly attributed to the two-dimensional effects resulting from the use of a high $I\lambda\sqrt{\tau}$ and a small laser spot, two parameters not well represented by ESTHER. The tendency of the code to overestimate the amount of liquid matter compared to 2D calculations could also explain part of the results. These observations will serve to guide future studies on momentum transfer by exploring, for example, parameters such as the laser spot size influence.

ACKNOWLEDGMENTS

We would like to thank the entire team at the Laboratoire d'Utilisation des Laser Intenses for allowing and helping us to carry out the experiments presented in this paper and providing us with samples. We would also like to thank the staff of the Gramat and Valduc CEA centers for kindly providing us with samples for the experiments.

AUTHOR DECLARATIONS

Conflict of Interest

The authors have no conflicts to disclose.

Author Contributions

C. Le Bras: Conceptualization (equal); Formal analysis (equal); Investigation (equal); Methodology (equal); Validation (equal); Visualization (equal); Writing – original draft (equal); Writing – review & editing (equal). **L. Berthe:** Data curation (equal); Formal analysis (equal); Resources (equal); Validation (equal); Writing – review & editing (equal). **L. Videau:** Data curation (equal); Formal analysis (equal); Methodology (equal); Software (equal); Writing – review & editing (equal). **S. Baton:** Data curation (equal); Investigation (equal); Resources (equal); Writing – review & editing (equal). **M. Boustie:** Conceptualization (equal); Data curation (equal). **S. Boyer:** Data curation (equal). **C. Rousseaux:** Data curation (equal). **E. Brambrink:** Data curation (equal); Writing – review & editing (equal). **J.-M. Chevalier:** Data curation (equal); Formal analysis (equal); Resources (equal); Validation (equal). **J. Houy:** Software (equal). **B. Aubert:** Data curation (equal); Writing – review & editing (equal). **B. Jodar:** Data curation (equal); Writing – review & editing (equal). **D. Loison:** Data curation (equal). **D. Hébert:** Conceptualization (equal); Data curation (equal); Formal analysis (equal); Funding acquisition (equal); Investigation (equal); Methodology (equal); Project administration (equal); Resources (equal); Supervision (equal); Validation (equal); Visualization (equal); Writing – review & editing (equal).

DATA AVAILABILITY

The data that support the findings of this study are available from the corresponding author upon reasonable request.

REFERENCES

[1]C. Bonnal, D. McKnight, C. Phipps, C. Dupont, S. Missonnier, L. Lequette, M. Merle, and S. Rommelaere, "Just in time collision avoidance–a review," Acta Astronaut. **170**, 637–651 (2020).
[2]N. Elfer, "Structural damage prediction and analysis for hypervelocity impacts: Handbook," Technical Report, 1996.
[3]A. E. Olshaker, "Experimental investigation in lead of the whipple"meteor bumper"," J. Appl. Phys. **31**, 2118–2120 (1960).
[4]B. G. Cour-Palais and J. L. Crews, "A multi-shock concept for spacecraft shielding," Int. J. Impact Eng. **10**, 135–146 (1990).
[5]B. Jodar, D. Hébert, B. Aubert, E. Andò, J.-L. Rullier, and I. Bertron, "Impacts into porous graphite: An investigation on crater formation and ejecta distribution," Int. J. Impact Eng. **152**, 103842 (2021).
[6]R. Destefanis, F. Schäfer, M. Lambert, and M. Faraud, "Selecting enhanced space debris shields for manned spacecraft," Int. J. Impact Eng. **33**, 219–230 (2006).
[7]A. N. Pirri, "Theory for momentum transfer to a surface with a high-power laser," Phys. Fluids **16**, 1435–1440 (1973).
[8]P. Nebolsine, "Laser simulation of hypervelocity impact," in *14th Aerospace Sciences Meeting* (AIAA, 1976), p. 52.
[9]A. N. Pirri, "Theory for laser simulation of hypervelocity impact," Phys. Fluids **20**, 221–228 (1977).
[10]J.-P. Bibring, F. Cottet, M. Hallouin, Y. Langevin, and J.-P. Romain, "Simulation laser d'impacts de particules de très grande vitesse," J. Phys. Lett. **44**, 189–194 (1983).
[11]G. Seisson, D. Hébert, I. Bertron, J.-M. Chevalier, L. Hallo, E. Lescoute, L. Videau, P. Combis, F. Guillet, M. Boustie, and L. Berthe, "Dynamic cratering of graphite: Experimental results and simulations," Int. J. Impact Eng. **63**, 18–28 (2014).
[12]B. Aubert, D. Hebert, J.-L. Rullier, E. Lescoute, L. Videau, and L. Berthe, "Simulation of laser-driven cratering experiments on aluminum," J. Laser Appl. **31**, 042014 (2019).
[13]A. Kantrowitz, "Propulsion to orbit by ground-based laser," Astronaut. Aeronaut. **10**, 74 (1972).
[14]C. Phipps, M. Birkan, W. Bohn, H.-A. Eckel, H. Horisawa, T. Lippert, M. Michaelis, Y. Rezunkov, A. Sasoh, W. Schall, S. Scharring, and J. Sinko, "Laser-ablation propulsion," J. Propul. Power **26**, 609–637 (2010).
[15]P. Battocchio, J. Terragni, V. Cristino, N. Bazzanella, R. Checchetto, M. Orlandi, S. Caramori, and A. Miotello, "Poly (vinyl chloride) coupling with uv laser radiation: Comparison between polymer absorbers and nanoparticles to increase efficiency for laser ablation propulsion," J. Phys. Chem. C **125**, 28088–28099 (2021).
[16]C. Phipps, W. Bohn, T. Lippert, A. Sasoh, W. Schall, and J. Sinko, "A review of laser ablation propulsion," AIP Conf. Proc. **1278**, 710–722 (2010).
[17]B. G. Cour-Palais, "Hypervelocity impact in metals, glass and composites," Int. J. Impact Eng. **5**, 221–237 (1987).
[18]C. Phipps, "Lisk-broom: A laser concept for clearing space junk," AIP Conf. Proc. **318**, 466–468 (2010).
[19]C. R. Phipps, J. R. Luke, T. Lippert, M. Hauer, and A. Wokaun, "Micropropulsion using laser ablation," Appl. Phys. A **79**, 1385–1389 (2004).
[20]C. Phipps, "An alternate treatment of the vapor-plasma transition," Int. J. Aerosp. Innovations **3**, 45–50 (2011).
[21]R. R. Rudder, "Air Force Weapons Laboratory Report No. AFWL-TR-74-100 (1974), available as ADD703343 from Defense Technical Information Center, Fort Belvoir, VA," 1974.
[22]J. McKay and P. Laufer, "Survey of laser-produced pressure and impulse data," Technical Report, Physical Sciences Inc, Alexandria, VA, 1988.
[23]C. Phipps, Jr., T. Turner, R. Harrison, G. York, W. Osborne, G. Anderson, X. Corlis, L. Haynes, H. Steele, K. Spicochi, and T. R. King, "Impulse coupling to targets in vacuum by KrF, HF, and CO_2 single-pulse lasers," J. Appl. Phys. **64**, 1083–1096 (1988).
[24]B. Arad, S. Eliezer, Y. Gazit, H. Loebenstein, A. Zigler, H. Zmora, and S. Zweigenbaum, "Burn-through of thin aluminum foils by laser-driven ablation," J. Appl. Phys. **50**, 6817–6821 (1979).
[25]C. R. Phipps, M. Boustie, J.-M. Chevalier, S. Baton, E. Brambrink, L. Berthe, M. Schneider, L. Videau, S. A. Boyer, and S. Scharring, "Laser impulse coupling measurements at 400 fs and 80 ps using the LULI facility at 1057 nm wavelength," J. Appl. Phys. **122**, 193103 (2017).

[26]M. Stimler, Z. Slawsky, and R. Grantham, "Torsion pendulum photometer," Rev. Sci. Instrum. **35**, 311–313 (1964).
[27]B. Lakatosh, D. Abramenko, V. Ivanov, V. Medvedev, V. Krivtsun, K. Koshelev, and A. Yakunin, "Propulsion of a flat tin target with pulsed CO_2 laser radiation: Measurements using a ballistic pendulum," Laser Phys. Lett. **15**, 016003 (2017).
[28]P. Battocchio, J. Terragni, N. Bazzanella, C. Cestari, M. Orlandi, W. Burger, R. Battiston, and A. Miotello, "Ballistic measurements of laser ablation generated impulse," Meas. Sci. Technol. **32**, 015901 (2020).
[29]P. D. Sargis, N. E. Molau, D. Sweider, M. Lowry, and O. Strand, "Photonic doppler velocimetry," United States, 1–6 (1999).
[30]O. T. Strand, D. Goosman, C. Martinez, T. Whitworth, and W. Kuhlow, "Compact system for high-speed velocimetry using heterodyne techniques," Rev. Sci. Instrum. **77**, 083108 (2006).
[31]J.-P. Colombier, P. Combis, F. Bonneau, R. Le Harzic, and E. Audouard, "Hydrodynamic simulations of metal ablation by femtosecond laser irradiation," Phys. Rev. B **71**, 165406 (2005).
[32]J. Cuq-Lelandais, M. Boustie, L. Berthe, T. De Rességuier, P. Combis, J.-P. Colombier, M. Nivard, and A. Claverie, "Spallation generated by femtosecond laser driven shocks in thin metallic targets," J. Phys. D: Appl. Phys. **42**, 065402 (2009).
[33]P. Leguay, A. Lévy, B. Chimier, F. Deneuville, D. Descamps, C. Fourment, C. Goyon, S. Hulin, S. Petit, O. Peyrusse *et al.*, "Ultrafast short-range disordering of femtosecond-laser-heated warm dense aluminum," Phys. Rev. Lett. **111**, 245004 (2013).
[34]S. Bardy, B. Aubert, T. Bergara, L. Berthe, P. Combis, D. Hébert, E. Lescoute, Y. Rouchausse, and L. Videau, "Development of a numerical code for laser-induced shock waves applications," Opt. Laser Technol. **124**, 105983 (2020).
[35]S. Bardy, B. Aubert, L. Berthe, P. Combis, D. Hébert, E. Lescoute, J.-L. Rullier, and L. Videau, "Numerical study of laser ablation on aluminum for shock-wave applications: Development of a suitable model by comparison with recent experiments," Opt. Eng. **56**, 011014 (2016).
[36]M. Scius-Bertrand, L. Videau, A. Rondepierre, E. Lescoute, Y. Rouchausse, J. Kaufman, D. Rostohar, J. Brajer, and L. Berthe, "Laser induced plasma characterization in direct and water confined regimes: New advances in experimental studies and numerical modelling," J. Phys. D: Appl. Phys. **54**, 055204 (2020).
[37]L. Spitzer, *Physics of Fully Ionized Gases* (Courier Corporation, 2006).
[38]A. Bushman and V. Fortov, "Wide-range equation of state for matter under extreme conditions," Sov. Tech. Rev. B **1**, 219 (1987).
[39]I. Lomonosov, A. V. Bushman, and V. E. Fortov, "Equations of state for metals at high energy densities," AIP Conf. Proc. **309**, 117–120 (1994).
[40]D. Steinberg, S. Cochran, and M. Guinan, "A constitutive model for metals applicable at high-strain rate," J. Appl. Phys. **51**, 1498–1504 (1980).
[41]J. N. Johnson, "Dynamic fracture and spallation in ductile solids," J. Appl. Phys. **52**, 2812–2825 (1981).
[42]E. D. Palik, *Handbook of Optical Constants of Solids* (Academic Press, 1998), Vol. 3.
[43]T. Moscicki, J. Hoffman, and Z. Szymanski, "The effect of laser wavelength on laser-induced carbon plasma," J. Appl. Phys. **114**, 083306 (2013).
[44]M. N. Saha, "LIII. Ionization in the solar chromosphere," London, Edinburgh, Dublin Philos. Mag. J. Sci. **40**, 472–488 (1920).
[45]K. Ujihara, "Reflectivity of metals at high temperatures," J. Appl. Phys. **43**, 2376–2383 (1972).
[46]M. W. Chase and National Institute of Standards and Technology, *NIST-JANAF Thermochemical Tables* (American Chemical Society, Washington, DC, 1998), Vol. 9.
[47]J. E. Sinko and C. R. Phipps, "Modeling CO_2 laser ablation impulse of polymers in vapor and plasma regimes," Appl. Phys. Lett. **95**, 131105 (2009).
[48]M. J. Burchell, M. J. Cole, J. McDonnell, and J. C. Zarnecki, "Hypervelocity impact studies using the 2 MV van de Graaff accelerator and two-stage light gas gun of the University of Kent at Canterbury," Meas. Sci. Technol. **10**, 41 (1999).
[49]P. Gupta, P. Naik, and H. Pant, "Effect of lateral energy transport on the momentum transfer to targets in laser produced plasmas," J. Appl. Phys. **56**, 785–789 (1984).